Supplementary Notes

Nonlinear elasticity degrades monolayer fracture toughness

Israel Greenfeld[†,*,#], Shenda Jiang[‡,#], Lin Yang[‡,*], H. Daniel Wagner[†,*]

[†]*Department of Molecular Chemistry and Materials Science, Weizmann Institute of Science, Rehovot 76100, Israel*

[‡]*Center for Composite Materials and Structures, Harbin Institute of Technology, Harbin 150080, China*

[#]These authors contributed equally to this work.

[*] Email: I.G. green_is@netvision.net.il, H.D.W Daniel.Wagner@weizmann.ac.il, L.Y. Linyang@hit.edu.cn

S1. Validation of the effectiveness of reactive force fields

S1.1 Development and application of reactive force field

In 2001 Duin et al. [1] developed a reactive force field for hydrocarbons based on first principles: ReaxFF. After training and development by Kim et al. [2] and Osti et al. [3] the reactive force field is now widely used in the study of mechanical properties and fracture behavior of $Ti_nC_{n+1}T_x$ MXene:

1. Yu et al. [4] used reactive force field to study the tensile mechanical properties and structural transformations of pristine Ti_2C and Ti_2C with different surface oxidation concentrations.

2. Deng et al. [5] used reactive molecular dynamics simulations to study the fracture behavior as well as friction and adhesion properties of pristine Ti_2C and surface oxidized Ti_2C under nanoindentation.

3. Wei et al. [6] investigated the anisotropic fracture behavior of MXene (Ti_2C and Ti_3C_2) with different monolayer thicknesses using reactive force field.

4. The in-plane and out-of-plane mechanical properties of $Ti_nC_{n+1}T_x$ have been explored in other literatures using a reactive force field [7-12].

ReaxFF is a force field used in molecular dynamics simulations and is particularly suitable for

characterizing chemical bond formation and fracture processes. It provides efficient and accurate simulations of chemical reactions through the relationship between bond order and bond energy and the inclusion of non-bonding interactions for a wide range of applications. The reaction force field decomposes the energy of the system into various partial energy contributions as shown in Eq. S1 [1]:

$$E_{\text{system}} = E_{bond} + E_{over} + E_{under} + E_{val} + E_{pen} + E_{tors} + E_{conj} + E_{vdWaals} + E_{\text{Coulomb}} \quad \text{(S1)}$$

Where E_{bond} is bond energy, E_{over} and E_{under} are over and under coordination energy, E_{val} is valance-angle energy, E_{pen} is penalty energy, E_{tors} is torsion-angle energy, E_{conj} is conjugation energy, $E_{vdWaals}$ is van der Waals energy, and $E_{Coulomb}$ is Coulomb energy.

S1.2 Parametric validation of reactive force field

The ReaxFF force field was originally parameterized for hydrocarbons and other related materials, and has been extensively trained and validated in subsequent studies for a wide range of MXene materials, including titanium-based. We chose this force field because it has demonstrated good accuracy in capturing the intra- and interlayer mechanical behavior of MXene structures, as cited in multiple studies [4-7]. Therefore, it is currently the most reliable option for Ti_2C simulations.

Although the reactive force field used in this paper has been applied to the study of the mechanical properties of Ti_2C, the accuracy of the force field has not been verified in this literature. The force field parameters of the reactive force field were developed for Ti_3C_2X MXene, a class of MXene with a different composition and chemical structure than the Ti_2C MXene discussed [3]. Therefore, the direct application of the parameters of the reactive force field to Ti_2C MXene may pose potential issues because the coordination environments of the elements may be different. For this reason, we performed a detailed validation of the accuracy and reliability of the reactive force field, as well as a comparison of the key mechanical parameters obtained by ReaxFF with those obtained by DFT and MD simulations reported in the literature. Specifically, we compared the lattice constants, thicknesses, cohesion energies, elastic constants (C_{11}, C_{12}, C_{22}), vacancy

formation energies of titanium and carbon atoms, and stress-strain curves of Ti_2C over the entire deformation range. The close agreement between these results supports the reliability of ReaxFF in predicting the mechanical behavior of Ti_2C MXenes.

It should be noted that the simulations of Ti_2C MXene using the ReaxFF force field were found to have some deviations in predicting the elastic constant C_{12}, the vacancy formation energy, and the behavior of the stress-strain curves over the entire deformation range. Specifically, the calculated results for C_{12} do not agree with typical values in the literature, the predicted values for the vacancy energy differ significantly between different literature results, and there are some errors in the prediction of the stress-strain curve in the high strain region and the failure stress. These deviations may raise concerns about the accuracy and reliability of the ReaxFF force field in modeling the mechanical behavior of Ti_2C MXene.

However, these deviations do not affect the reliability of ReaxFF in predicting the mechanical behavior of Ti_2C MXenes, which is the focus of the current study, for the following reasons:

(1) Influence of the elastic constant C_{12}: Although the predictions of C_{12} deviate from typical values in the literature (the force field is deficient in capturing the transverse deformation), the effect of C_{12} on the overall mechanical behavior is limited in uniaxial stretching studies. C_{12} is mainly correlated with Poisson's ratio, which is not dominant in describing the stress-strain relationship in uniaxial stretching. More importantly, ReaxFF performs well in predicting the other key elastic constants C_{11} and C_{22}, which are parameters that more directly determine the response of a material under uniaxial stretching. Therefore, deviations in C_{12} do not significantly affect the overall mechanical behavior of Ti_2C predicted by the ReaxFF force field.

(2) Differences in vacancy formation energies: Although the results of vacancy formation energy calculations vary significantly across the literature, this can be largely attributed to the different calculation methods and parameter settings used in the individual studies. ReaxFF performs consistently in predicting relative trends (e.g., the relative values of vacancy energies for Ti and C atoms), which suggests that it is still reliable in modeling the effects of material defects on mechanical behavior.

(3) Deviation of stress-strain curves in the high strain region: the linear elasticity and initial nonlinear deformation behavior of Ti_2C were accurately captured by ReaxFF at low temperatures. Although there are some prediction deviations in the high strain region, these deviations can be effectively compensated by introducing a criterion for the maximum critical fracture stress (e.g., the maximum bond strength of the Ti-C bond) based on DFT calculations. This criterion ensures the accuracy of the simulation results at critical fracture points and enables the ReaxFF force field to reliably predict the mechanical behavior of Ti_2C. This fracture criterion is described in detail in Section S2.

The comparison and validation results are presented in Table S1 and Figure S1.

Table S1. The lattice constant a, monolayer thickness t, cohesion energy E_c, elastic constants C_{11} and C_{22} associated with uniaxial stretching, vacancy formation energies of Ti atoms, and vacancy formation energies of C atoms of pristine Ti_2C calculated using a reactive force field, compared with the results of DFT and MD simulations from the relevant literatures.

Parameters	This work	DFT	MD
a (Å)	3.06	3.08 [13], 3.04 [14], 3.03 [15]	2.95 [16]
t (Å)	2.29	2.30 [15], 2.31 [14], 2.29 [17]	2.35 [16]
E_c (eV/atom)	-6.56	-6.17 [16]	-6.34 [16], -6.22 [18]
C_{11} (N/m)	155.67	151 [19], 145 [16], 137 [20]	152 [4], 149.46 [16]
C_{22} (N/m)	155.19	153 [19], 135 [21]	149 [4]
C_{12} (N/m)	-1.05	35 [19], 32 [20], 38.346 [16]	35.25 [16]
E^f_{Ti} (eV)	1.51	2.92 [22], 8.071 [23], 2.35 [24], 7.71 [16]	8.64 [16]
E^f_C (eV)	3.56	3.06 [22], 12.01 [23], 2.86 [24], 10.64 [16]	11.37 [16]

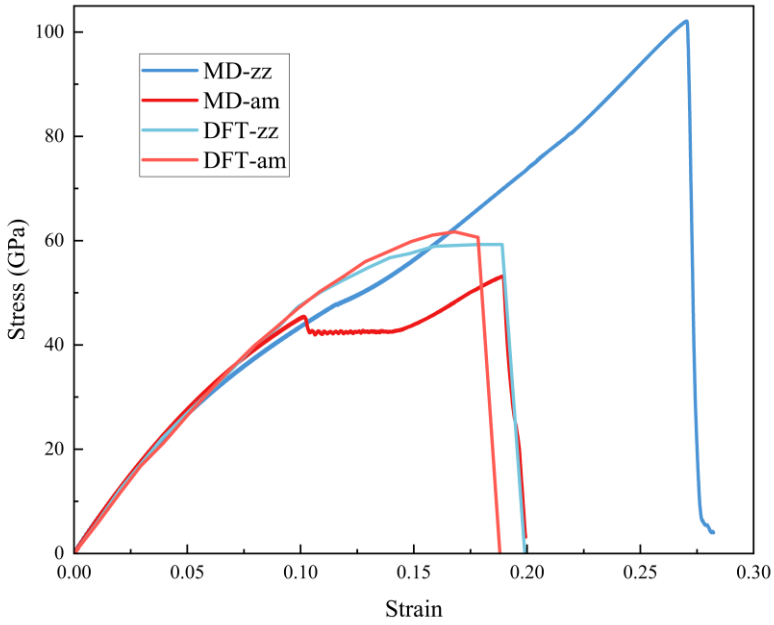

Figure S1. Comparison between the stress-strain curves simulated in this paper (at a temperature of 10°K) and the results from DFT [13].

In summary, although the ReaxFF force field has biases in predicting some specific parameters, these biases do not significantly affect its reliability in modeling the overall mechanical behavior of Ti_2C MXene. With reasonable complementary methods (e.g., maximum critical fracture stress criterion) and accurate prediction of key parameters, the ReaxFF force field remains the best tool currently available for studying the mechanical behavior of Ti_2C MXene. The applicability of the ReaxFF force field was validated in this work, particularly in the low strain region which is relevant to the investigation of fracture in the presence of embedded defects. In the high strain region, which is not relevant to this study once a maximum stress fracture criterion is introduced (see Section S2), further optimization of the force field or incorporation of other computational methods are still needed in future research efforts.

S2. Selection of fracture criterion

Before exploring the effect of defects on the fracture mechanism of monolayer Ti_2C, we simulated uniaxial tensile tests (at 10°K and 300°K) along two orthogonal directions on both the

original Ti_2C and the Ti_2C structures containing defects of different lengths. The results are displayed in Figures S2 and S3. To simplify the analysis, we divided the models into two groups stretched along the sawtooth direction (x-direction) and the armchair direction (y-direction). In order to show the results clearly, we only show the original Ti_2C and the defect models with 1, 3, 5, and 7 missing atoms. Refer to definition of the directions in Figure 1.

From Figure S2, it can be seen that when stretched along the x-direction, Ti_2C exhibits brittle fracture at both 10°K and 300°K. From Figure S3, it can be found that when stretched along the y-direction, Ti_2C similarly exhibits brittle fracture at 300°K. The Ti_2C is also characterized by brittle fracture when stretched along the y-direction. However, the pristine Ti_2C and the defective model with 1 missing atom exhibited a plastic deformation phase after 0.1 strain when the temperature was 10°K. A similar phenomenon was observed in the calculations published by Yu et al. [4]. It should be noted, however, that in situ tensile tests of monolayers of $Ti_3C_2T_x$ at room temperature indicate that such materials exhibit brittle fracture characteristics.

Therefore, we speculate that this plastic deformation behavior may be caused by the anomalous behavior of the reactive force field when simulating pristine Ti_2C at low temperatures in the armchair y-direction. To verify this speculation, we simulated uniaxial tensile tests along the y-direction on all the defect models, and all of them exhibited brittle fracture except for the defect model with one missing atom, which exhibited plastic deformation behavior. This suggests that there is indeed some bias in simulating the fracture behavior of Ti_2C at low temperatures using the reaction force field. From the comparison of MD and DFT in Figure S1, it can be seen that the reactive force field captures the linear-elastic and nonlinear deformation behaviors of Ti_2C well at low temperatures, but there is some bias in predicting the failure stress and the stress-strain curve after 0.1 strain.

It is important to note that low-temperature simulations are common practice when using molecular dynamics simulations to study the fracture of two-dimensional materials [4, 6, 11, 25]. This is due to the fact that more accurate stress distributions can be obtained at low temperatures and the effect of thermal fluctuations on atomic level fracture of brittle materials can be eliminated.

In contrast, the stress states obtained at higher temperatures are too cluttered to give a clear and effective picture of the stress distribution and fracture mechanism of Ti_2C. Therefore, there is a certain inconsistency between the low temperature and the accuracy of the reactive force field when studying the fracture mechanism of Ti_2C.

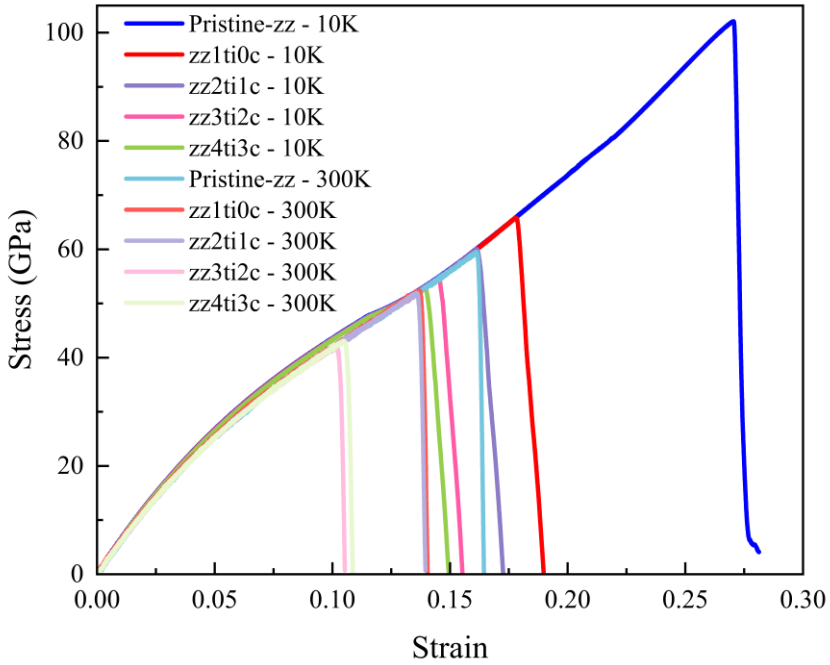

Figure S2. Stress-strain curves of partial Ti_2C models stretched along the x direction at different temperatures

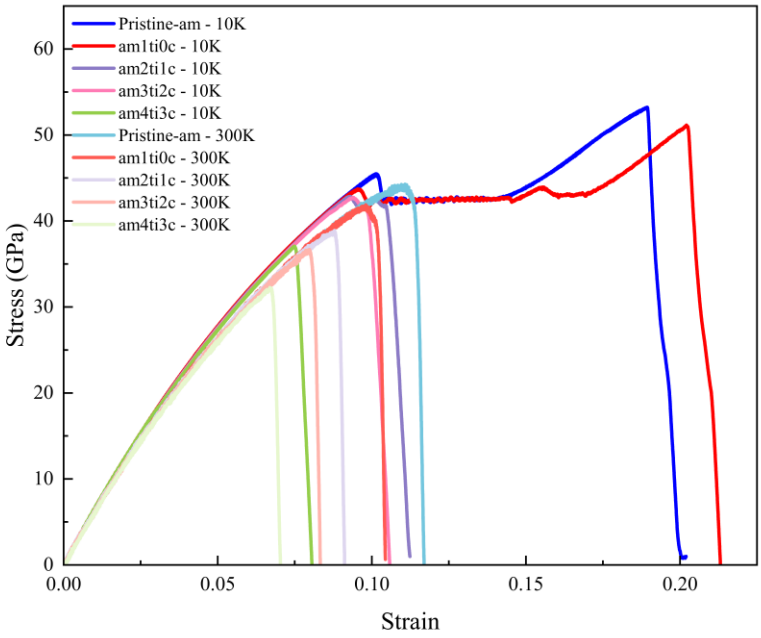

Figure S3. Stress-strain curves of partial Ti_2C models stretched along the y direction at different temperatures

To resolve this issue, we refer to the studies on brittle fracture modeling of graphene by Yin et al. [25] and fracture mechanics modeling of carbon nanotubes by Yang et al. [26]. Yin pointed out that the crack extension of graphene may be determined by the strength of the atomic bonds (i.e., the critical stress at the tip of the crack that tears the graphene), rather than the edge energy. Yang et al., by using the equivalent maximal bonding force in place of the bond dissociation energy, proposed a critical fracture criterion for carbon nanotubes.

Furthermore, the notion of a critical fracture stress criterion is extensively formulated in fracture mechanics theory and applications (Anderson, ed.) [27] as follows:

1. Material fracture criterion: A material will fracture when sufficient stress and work are applied at the atomic level to break the bonds that hold the atoms together.

2. Defect effects in materials: the difference between the actual strength of a brittle material and the theoretical estimate is usually caused by defects in the material. Fracture occurs only when the stress at the atomic level exceeds the cohesive strength of the material. Defects reduce the overall strength by locally amplifying the stress.

3. Localized failure criterion in macroscopic fracture analysis: A maximum stress criterion, similar to the one presented in this paper, is applied to macroscopic finite element analysis, whereby a cohesive small element behaves in the same way as the breaking of a covalent bond in a molecular dynamics simulation.

Therefore, we introduce the maximum critical fracture stress criterion in our study to resolve the inconsistency between the low-temperature simulation and the accuracy of the reaction force field. Based on the DFT results in Figure S1, we define the maximum critical fracture stress (the maximum bond strength of the Ti-C bonds) to be 60 GPa, which is used to determine whether the Ti-C bonds at the tip of a defect exceed their strength. It is important to note that the disruption of a single Ti-C bond does not necessarily mean that fracture will occur because once one bond is disrupted, the load is transferred to the other bonds. Thus, if the stress is higher than the strength of the subsequent bond, the crack will continue to extend. Conversely, if the local stress is lower than the strength of that bond, the crack will not extend. See also the crack instability analysis using

the J integral approach in Section S5. By introducing the maximum critical fracture stress criterion, we have successfully compensated for the deviation of the reactive force field in predicting the Ti_2C failure stress and the stress-strain curve after 0.1 strain, which makes the calculation of the reactive force field in agreement with the DFT results. Upon applying the maximum critical fracture stress criterion, the resulting critical fracture strains of various defected structures are presented in Table S2, showing that the critical strains are predominantly below 10%.

Table S2. Critical fracture strain of various defected structures under the maximum critical fracture stress criterion at 10°K.

Vacancy type	Critical strain-x	Vacancy type	Critical strain- y
pristine-zz	0.13	pristine-am	0.176
am-1ti0c	0.1152	zz-1ti0c	0.1524
am-1ti1c	0.0984	zz-1ti1c	0.0858
am-2ti1c	0.1002	zz-2ti1c	0.079
am-2ti2c	0.0832	zz-2ti2c	0.0698
am-3ti2c	0.0752	zz-3ti2c	0.0672
am-3ti3c	0.0706	zz-3ti3c	0.061
am-4ti3c	0.0732	zz-4ti3c	0.06
am-4ti4c	0.0628	zz-4ti4c	0.0546
am-8ti8c	0.048	zz-6ti6c	0.0458
am-16ti16c	0.032	zz-12ti12c	0.0342
am-24ti24c	0.026	zz-18ti18c	0.0282
am-48ti48c	0.0188	zz-36ti36c	0.0196
am-64ti64c	0.0158	zz-48ti48c	0.0174

S3. Effect of Temperature on the Mechanical Response of Pristine MXene

The overall mechanical response of the pristine Ti_2C monolayer at 0°K, 10°K, and 300°K is

shown in Figure S4. It can be observed that, due to minimal thermal fluctuations, the mechanical responses of Ti_2C at 0°K and 10°K exhibit little difference. At 300°K, as atomic thermal fluctuations intensify, the fracture strain and strength decrease significantly, resulting in a pronounced difference in mechanical response compared to lower temperatures. However, we emphasize that, upon applying the maximum critical fracture stress criterion as justified in Section S2 above, the strain range of interest for the purpose of this study is primarily within 10%, and in that range the difference in stress-strain response between 300°K and 0°K is small.

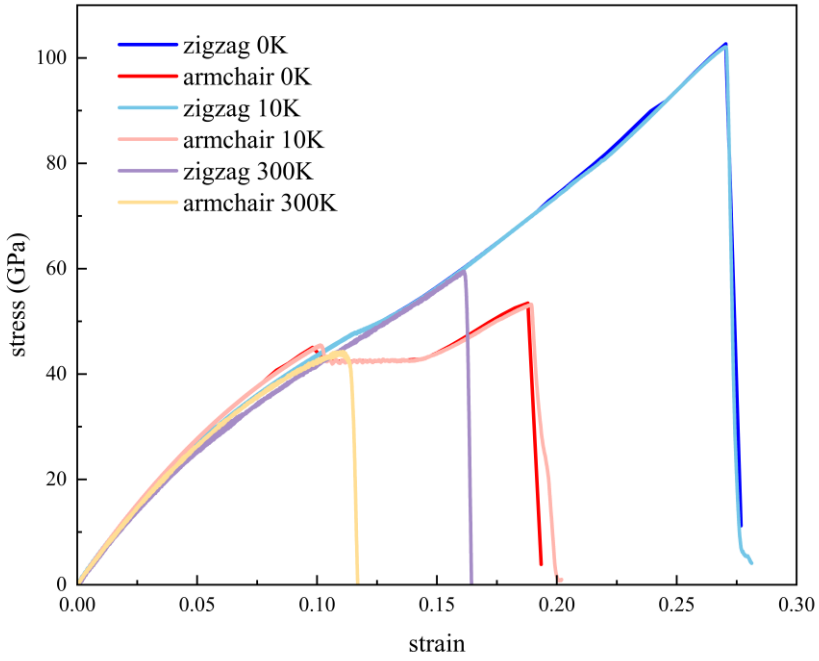

Figure S4. Stress-strain curves of pristine MXene along different chiral directions at various temperatures.

S4. Justification for using fracture mechanics in monolayers

S4.1 Validity of fracture modeling

In fracture mechanics, crack propagation is fundamentally driven by the release of stored elastic energy, which destabilizes the crack. When the elastic strain energy released during crack propagation exceeds the material's resistance, the crack will extend. This theoretical framework applies not only to materials at the macroscopic scale but also to discrete atomic structures at the nanoscale [27]. At the atomic scale, although material behavior exhibits discreteness and complex

interactions, the storage and release of elastic energy remain the core mechanisms driving crack formation and propagation. Therefore, fracture mechanics (FM) theories, including linear (LEFM), nonlinear (NLFM), and quantized (QFM), as well as their combination used in this study, all revolve around this fundamental principle of energy balance, providing a unified theoretical foundation for understanding fracture behavior from the macroscopic to the atomic scale.

The sudden fracture of materials such as MXene and graphene is typically brittle, resulting from either gradual or rapid crack propagation. At macroscopic and mesoscopic scales, the study of brittle fracture is well-established, and such problems can often be addressed using linear elastic fracture mechanics (LEFM). However, with the recent advances in miniaturization of mechanical structures and electronic components, fracture issues at the nanoscale have become increasingly important. When the material dimensions shrink to the nanoscale, the assumptions of LEFM—such as linear elasticity, isotropy, and constant surface energy—may no longer hold. At this scale, factors such as the discreteness and anisotropy of atomic structures, non-uniformity of stress fields, and nonlinearity of interatomic interactions become critical and cannot be neglected. Therefore, at the nanoscale, determining the applicability of LEFM and applying other theories to describe the fracture of nanoscale materials are key challenges.

Fracture mechanics has been applied extensively to monolayers and nanoparticles, as already noted in the main text (see the Introduction and Section 3.6, including citations thereof). Recently, several studies have reported significant deviations between simulation results at the nanoscale and fracture mechanics theories for materials such as silicon, graphene, and MoS_2 [25, 28-32]. These findings suggest the existence of a critical scale below which linear elastic fracture mechanics (LEFM) may not always be applicable. Consequently, it is crucial to analyze the atomic-scale fracture mechanisms of nanomaterials in detail and to establish other theories capable of accurately describing fracture behavior at the nanoscale.

Through our molecular dynamics simulations of MXene, we identified that LEFM, while capable of predicting the fracture stress in the presence of long defects, fails to predict the fracture stress for short defects. We found that this is primarily due to the non-uniformity of the stress field,

the nonlinearity of interatomic interactions, and the discreteness of atomic structures. Based on these observations, we analyzed the applicability of nonlinear fracture mechanics (NLFM) [33] and quantized fracture mechanics (QFM) [34] to the fracture behavior of MXene. While these two fracture mechanics theories, which account for individual influencing factors, each perform better than LEFM, they still fail to fully and accurately describe the fracture behavior of MXene at the nanoscale.

By comprehensively considering the specific fracture mechanisms of MXene and the reasons for the failure of LEFM, we developed a model that integrates NLFM and QFM. This model simultaneously accounts for nonlinear mechanical responses and the discretization of atomic structures, making it well-suited for describing the fracture behavior of MXene. Most importantly, it accurately predicts the maximum stress at failure for MXene containing short cracks, and avoids the non-physical stress divergence predicted by LEFM.

As noted, our fracture mechanics model incorporates quantized fracture mechanics (QFM), which is well-suited for application in discrete nanoscale scenarios, and was validated on several such systems [34, 35]. Within the framework of the continuum hypothesis, QFM successfully introduces the concept of "quantized" stress by replacing the differential form in Griffith's criterion with a finite difference approach. This enables QFM to describe the fracture behavior of small-scale, discrete systems. By accounting for the discreteness of atomic structures, QFM overcomes the limitations of classical fracture mechanics in cases involving extremely small cracks and modifies the LEFM model to accommodate material heterogeneity and atomic-scale discontinuities.

To conclude, the fracture mechanics approach developed in this study combines the separate effects of nonlinear elasticity and quantization, both inherent properties of the MXene monolayer. While each of these effects is, in itself, not sufficient for describing the fracture behavior of MXene as simulated by molecular dynamics, their integration in a unified model describes well the MXene’s discrete nanoscale structures containing defects, and is thus justified.

S4.2 Modeling assumptions and limitations

The assumptions and potential limitations of applying these theoretical fracture mechanics models on molecular dynamics results are discussed in the following items. As a general note that applies to most of the items below, this study is primarily concerned with the condition for initiation of defect instability in a quasi-static scenario, and therefore dynamic behavior induced by crack propagation was irrelevant for the analysis.

1. This study adopts the maximum critical fracture stress criterion, assuming that a crack becomes unstable when the maximum stress at its tip reaches the theoretical strength. While this assumption is effective for describing crack initiation, it has limitations in capturing the complex stress fields at the crack tip and the subsequent propagation behavior. Additional details and justification are provided in Note S2 above.

2. The simulations are conducted at zero temperature, a simplification that helps eliminate the effects of thermal fluctuations on the structural stress field. However, this assumption neglects the influence of temperature and thermal effects on fracture stress and strain. Particularly under high-temperature or dynamic loading conditions, this simplification may lead to deviations between the results and real-world behavior. We note that, within the low range of critical strains, which is relevant to the current study, the effect of temperature on the mechanical behavior is small. Additional details and justification are provided in Section 2.2 in the main text and in Note S3 above.

3. The introduced quantized fracture mechanics (QFM) framework describes discrete crack propagation behavior through finite differences, and it is primarily suitable for predicting crack initiation. QFM was validated on several atomic structures [34, 35] – see more information and justification in Section S4.1 above. Because QFM recovers continuity by averaging the stress intensity over a distance of atomic scale (the fracture quantum), it cannot account for the complex dynamic behavior at crack tips, and is less effective in predicting subsequent crack propagation.

4. The nonlinear fracture mechanics introduced in this study applies the Ramberg-Osgood equation to express the nonlinear elasticity of MXene. This equation assumes bulk, isotropic

material and was validated mostly on metals, whereas the MXene is extremely thin and locally anisotropic. However, at a scale above the local atomic scale and for a fracture strain below 10%, our MD results show that the elastic and fracture behavior of the MXene are almost isotropic, as they are nearly the same in armchair and zigzag directions (see figures 1b and 5a in the main text). Locally, at atomic scale, the MXene is evidently anisotropic, but this does not affect the analysis because the Ramberg-Osgood equation is used to calculate the released elastic energy which is spread over a significant region around the crack. This potential limitation might be relevant for very small defects where the region of released energy is also very small, an interesting subject for future investigation. It is also worth noting that the Ramberg-Osgood equation is over-parameterized [27]. To reduce model complexity and simplify fitting, we set α = 1. The very high accuracy of the fit ($R^2 > 0.9999$) to the stress-strain behavior captured by the MD provides confidence in this approach. Additional details are provided in Section 3.1 in the main text.

5. When deriving the specific expression for nonlinear fracture mechanics, the volume of the region from which the elastic energy was released was approximated as $2\pi a^2 B$. This approach simplifies the calculation of the elastic energy released by the defected plate but may overlook the influence of the material's microstructure on the results. This approximation is validated by the more general J integral method (presented in Note S5 below). Additionally, the critical defect length was determined using a Taylor series expansion, where higher-order terms were neglected, potentially introducing deviations. That said, after incorporating QFM, the model exhibits excellent fit to the fracture data, as seen in Figure 6 in the main text. Furthermore, the analysis in Note S5 presents the exact value of J, the strain energy released rate, as function of the crack length, geometry and applied stress.

6. The fracture mechanics model presented in this study was developed under uniaxial tensile loading conditions and is therefore not applicable to the fracture behavior of materials under more complex loading conditions, such as multiaxial loading or compressive-shear modes. However, it allows insight into the basic fracture behavior and properties of MXene. Furthermore, the J integral modeling in Section S5 may be adapted to various loading and geometry configurations that are

provided in the literature [27].

S5. MXene fracture toughness using J-integral

In the main text, we used the classic Griffith and Irwin approach for calculating the fracture toughness of MXene with nonlinear elasticity. In the following analysis, the more general J integral method is presented, which applies to nonlinear elasticity as well as to plasticity. J is the strain energy release rate, that is, the amount of energy released per unit area of an incremental increase in crack surface. The analysis is based on Anderson [27] chapters 3.2 and 9.3. The nonlinear elasticity (and plasticity, if relevant) are described by the empirical Ramberg-Osgood equation (Eq. (1)) [27, 36].

For the linear elastic part, $J_l = G$, where G is the cohesive fracture energy per unit crack area. Using the Griffith solution (Eq. (6)):

$$J_l = \frac{\pi h \sigma^2 a}{E} \tag{S2}$$

where σ is the far-field (applied) stress, a is the crack half length, and E is the modulus (slope of the stress-strain curve at the origin). The parameter h is a geometry correction factor, which depends on the ratio a/w, where w (or L in Figure 2) is the monolayer half-width ($h = 1$ when $a \ll w$) [37].

For the nonlinear elastic (or plastic, if relevant) part, we use the EPRI (Electric Power Research Institute) engineering approach, specifically the configuration described in Anderson Table 9A.11 for middle tension (MT) plate in plane stress:

$$J_{nl} = \frac{\alpha \sigma_0^2 a}{E} \left(1 - \frac{a}{w}\right)^{-n} h_1 \left(\frac{\sigma}{\sigma_0}\right)^{n+1} \tag{S3}$$

where the substitutions $b = w - a$ and $\varepsilon_0 = \sigma_0/E$ were used. σ_0 is a reference stress, and n is a strain hardening/softening exponent. The geometry correction factor h_1 is given in Anderson Table 9A.11, depending on the ratio a/w and the exponent n.

The total J is obtained by adding the linear and nonlinear parts and rearranging [27]:

$$J = J_l + J_{nl} = \frac{\pi \sigma^2 a}{E} \left[h + \frac{\alpha}{\pi} h_1 \left(1 - \frac{a}{w}\right)^{-n} \left(\frac{\sigma}{\sigma_0}\right)^{n-1} \right] \tag{S4}$$

For the Ti_2C MXene nonlinear elasticity described by Eq. (1), we have, $\alpha = 1$, $n = 3$ (equivalent to $m = 2$), and $a \ll w$, and therefore:

$$J = \frac{\pi\sigma^2 a}{E}\left[1 + \frac{h_1}{\pi}\left(\frac{\sigma}{\sigma_0}\right)^2\right] \tag{S5}$$

The term $h_1/\pi \cong 1.62$ for these parameters, obtained by extrapolation of the data in Anderson Table 9A.11. Equations (S4) and (S5) compare well with Eq. (8) when G is replaced by J (the prefactor for the nonlinear part is 1.5 compared to 1.62, respectively). The material resistance, J_R, is given for critical defects by setting $\sigma = \sigma_f$, the far-field fracture stress:

$$J_R \cong \frac{\pi\sigma_f^2 a}{E}\left[1 + \frac{h_1}{\pi}\left(\frac{\sigma_f}{\sigma_0}\right)^2\right] \tag{S6}$$

Using Eqs. (S5) and (S6) with the MXene MD results from the main text, the driving force J curves and the resistance J_R curves are depicted in Figure S5 for both armchair and zigzag defects. The J_R resistance curves exhibit a sharp rise with increasing defect length, and then level, tending to a critical value J_{Ic} (about 5.2 J/m^2 for zigzag defects). This critical value relates to sheets with long defects under low stress, a domain where the material is nearly linear elastic (see Figure 1). By comparison, in the J integral calculation by Wei et al. [6], carried out for compact tension loading of Ti_2C by integrating along a closed path around the crack tip, the J_{Ic} values of 35 J/m^2 (AC) and 55 J/m^2 (ZZ) were obtained; the large difference with respect to our results, which were obtained for middle tension loading, may be due to the different tensile configuration as well as to the different analysis method and fracture criterion.

For crack growth to be stable, the rate of change of the driving force with respect to crack length should be lower than or equal to that of the resistance, that is, $\frac{\partial J}{\partial a} \leq \frac{\partial J_R}{\partial a}$ [27]. This condition is first met around $\sigma = 50$ GPa close to the smallest possible defect (single missing atom). When the driving force is above that value, a crack will propagate from the initial defect until failure and is therefore unstable. For a lower driving force, for example when $\sigma = 30$ GPa, a defect shorter than about 7Å will not propagate and is therefore stable, whereas a longer defect will propagate as a crack until failure and is therefore unstable.

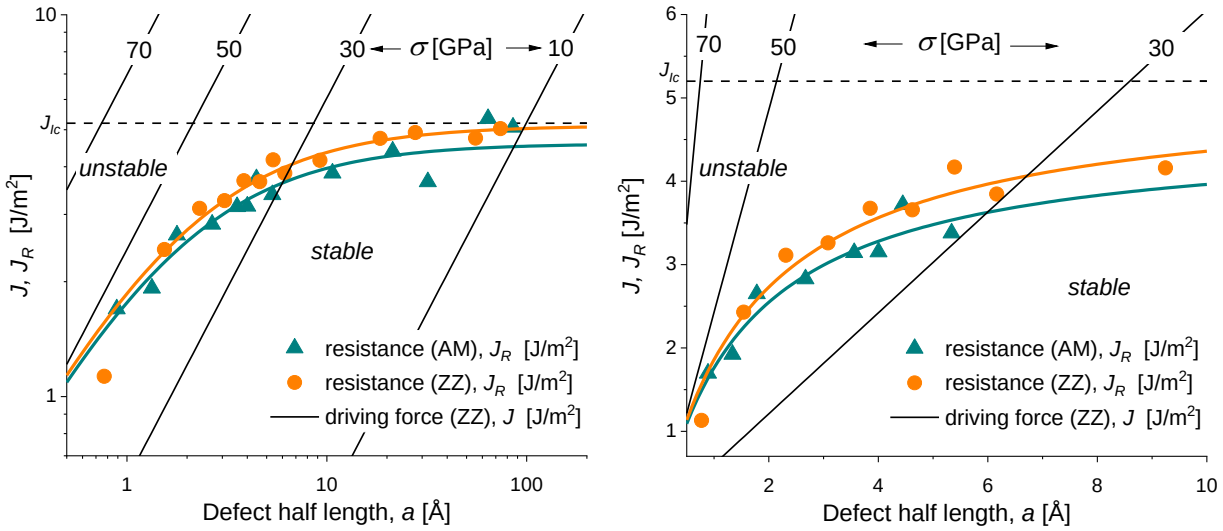

Figure S5. Crack instability analysis. J_R resistance curves for armchair and zigzag defects, using the material and fracture data from the MD simulation (Eq. (S6)). J driving force curves for zigzag defects for four values of the applied far-field stress σ (Eq. (S5)). The defect is assumed to be much smaller than the sheet width ($a \ll w$). The plot on the left is log-log, whereas the plot on the right is linear with magnification of the small defects region.

S6. Estimate of fracture toughness by bonding energy

For the purpose of validating the results obtained by fitting the strength (Figure 6), the fracture toughness may be estimated in a different way using the relation $K_{Ic} = \sqrt{EG}$ (Eq. (6)), which is valid for sufficiently long defects. The energy to remove a single atom is calculated by $U_{vf} = U_v - U_{perf} + U_w$, where U_v denotes the total energy of the system containing one vacancy, U_{perf} denotes the total energy of the system without defects, and $U_w = U_{perf}/N$ denotes the energy of the removed atom, N being the number of atoms in the pristine system [24, 38]. The fracture energy of a C atom is different (higher) than a Ti atom, as C has 6 Ti-C bonds whereas Ti has 3 bonds. To avoid this variability, and to account for atoms removal at the edge of an existing defect, the fracture energy was averaged over 4 atoms by removing atoms from a 2ti2c defect to obtain a 4ti4c defect.

Using these definitions, the calculated average energy to remove an atom is 32.8 kcal/mol (armchair) and 35.3 kcal/mol (zigzag). Dividing these energies by the increase in the defect area due to an atom removal, qt, where q is the defect added length (Eq. (13)) and $t = 2.31$Å is the MXene thickness [14, 39], we get the fracture energies $G_{AC} = 7.40$ J/m^2 and $G_{ZZ} = 6.89$ J/m^2.

Using the moduli at low strain obtained by Eq. (1), the calculated fracture toughness is $K_{Ic} = 2.15$ MPa·m$^{0.5}$ for an armchair defect and $K_{Ic} = 2.10$ MPa·m$^{0.5}$ for a zigzag defect, in the ballpark of the values obtained by fitting the strength data (Figure 6). By comparison, using MXene vacancy formation energies from the literature (2-3 eV per single-atom vacancy) [40], the prediction for K_{Ic} would be about 30% smaller.

S7. Correction for blunt cracks

QFM offers a correction for blunt cracks by applying the factor $\sqrt{1 + \rho/2q}$ to Eq. (12). Thus, the fracture toughness of a blunt defect is given by [34]:

$$K'_{Ic} \approx K_{Ic}\sqrt{1 + \frac{\rho}{2q}}, \qquad \text{QFM} \tag{7}$$

assuming small values of ρ/q. Using this factor in the strength fit, we obtain the same QFM trendline as in Figure6b, which aligns well with the long-defects data, with the effect of reducing the toughness prediction for a sharp defect, K_{Ic}, by the same factor. For example, using a defect tip radius $\rho = q/2$, the resulting factor has the effect of reducing K_{Ic} of a sharp defect by a factor of 1.12, without impact on the trend of the predicted strength. This factor can be applied to the NLFM+QFM model (Eq. (14)) as well, with the same impact on the fracture toughness. The value of ρ is uncertain in view of the irregular shape of the tip of an atomic defect (see also the very large value of ρ obtained by fitting the stress concentration in Figure5c), and therefore this blunt-defect factor was not applied in our analysis.

S8. Effect of prestresses on nonlinearity

Figure S6 demonstrates the effect of a prestress on the nonlinear behavior of the local stress. The local stress at the defect tip (red line) starts with a positive bias of the magnitude of the tensile prestress (about 18 GPa in this example), then rises moderately with the far-field strain, eventually

rising at a rate corresponding to a structure without prestress (the dashed line). The outcome is a nonlinear stress-strain elastic behavior.

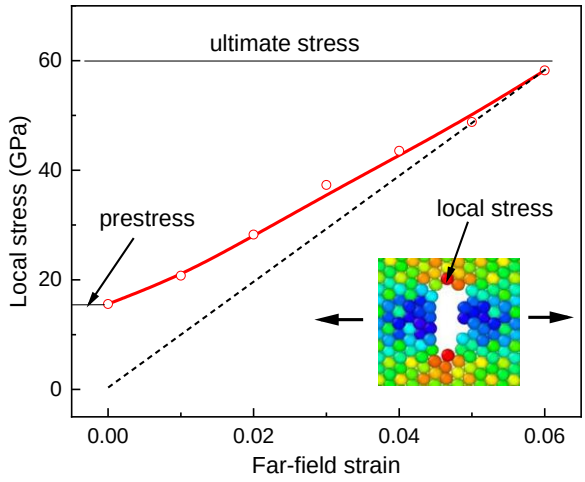

Figure S6. Simulated local stress at the tip of an armchair 4ti4c defect vs. the far-field strain. The local sress asymptote is depicted by a dashed line. The prestress and ultimate stress are indicated.

References

[1] A.C. Van Duin, S. Dasgupta, F. Lorant, W.A. Goddard, ReaxFF: a reactive force field for hydrocarbons, The Journal of Physical Chemistry A 105(41) (2001) 9396-9409.

[2] S.-Y. Kim, N. Kumar, P. Persson, J. Sofo, A.C. Van Duin, J.D. Kubicki, Development of a ReaxFF reactive force field for titanium dioxide/water systems, Langmuir 29(25) (2013) 7838-7846.

[3] N.C. Osti, M. Naguib, A. Ostadhossein, Y. Xie, P.R. Kent, B. Dyatkin, G. Rother, W.T. Heller, A.C. Van Duin, Y. Gogotsi, Effect of metal ion intercalation on the structure of MXene and water dynamics on its internal surfaces, ACS applied materials & interfaces 8(14) (2016) 8859-8863.

[4] H. Yu, K. Xu, Z. Zhang, X. Cao, J. Weng, J. Wu, Oxygen functionalization-induced crossover in the tensile properties of the thinnest 2D Ti 2 C MXene, Journal of Materials Chemistry C 9(7) (2021) 2416-2425.

[5] Y. Deng, Y. Chen, H. Liu, X. Yan, The effects of the temperature and termination (-O) on the friction and adhesion properties of MXenes using molecular dynamics simulation, Nanomaterials 12(5) (2022) 798.

[6] C. Wei, C. Wu, Nonlinear fracture of two-dimensional transition metal carbides (MXenes), EnFM 230 (2020) 106978.

[7] Y.I. Jhon, Y.T. Byun, J.H. Lee, Y.M. Jhon, Robust mechanical tunability of 2D transition metal carbides via surface termination engineering: molecular dynamics simulation, Appl. Surf. Sci. 532 (2020) 147380.

[8] Y. Chen, S. Tang, X. Yan, Manipulating the crack path through the surface functional groups of MXenes, Nanoscale 14(38) (2022) 14169-14177.

[9] Y.I. Jhon, I.K. Han, J.H. Lee, Y.M. Jhon, Microscopic understanding of exceptional orientation-dependent tensile and fracture responses of two-dimensional transition-metal carbides, Appl. Surf. Sci. 585 (2022) 152557.
[10] Y.I. Jhon, J.H. Lee, Tailoring mechanical properties of MXenes by composition ratio control of surface terminations: Reactive molecular dynamics simulation, Computational Materials Science 227 (2023) 112268.
[11] L. Miao, C. Sui, W. Hao, Y. Zhao, G. Zhao, J. Li, J. Li, G. Cheng, Y. Sang, C. Zhao, High Impact Resistance of 2D MXene with Multiple Fracture Modes, Nano Lett. 23(19) (2023) 9065-9072.
[12] G. Plummer, B. Anasori, Y. Gogotsi, G.J. Tucker, Nanoindentation of monolayer Tin+ 1CnTx MXenes via atomistic simulations: The role of composition and defects on strength, Computational Materials Science 157 (2019) 168-174.
[13] Z. Guo, J. Zhou, C. Si, Z. Sun, Flexible two-dimensional Ti n+ 1 C n (n= 1, 2 and 3) and their functionalized MXenes predicted by density functional theories, Physical Chemistry Chemical Physics 17(23) (2015) 15348-15354.
[14] N. Zhang, Y. Hong, S. Yazdanparast, M.A. Zaeem, Superior structural, elastic and electronic properties of 2D titanium nitride MXenes over carbide MXenes: a comprehensive first principles study, 2D Materials 5(4) (2018) 045004.
[15] Y. Bai, K. Zhou, N. Srikanth, J.H. Pang, X. He, R. Wang, Dependence of elastic and optical properties on surface terminated groups in two-dimensional MXene monolayers: a first-principles study, RSC advances 6(42) (2016) 35731-35739.
[16] G. Plummer, S. Thomas, M. Asle Zaeem, G.J. Tucker, Bond-order potential for the surface-terminated titanium carbide MXene monolayers Ti n+ 1 C n T x (n= 1, 2, or 3; T=-O or-F), Physical Review B 106(5) (2022) 054105.
[17] M. Kurtoglu, M. Naguib, Y. Gogotsi, M.W. Barsoum, First principles study of two-dimensional early transition metal carbides, Mrs Communications 2 (2012) 133-137.
[18] M.M. Hassan, J. Islam, W.R. Sajal, M.N.H. Noman, M.A. Rahman, Atomistic simulation of the mechanical behaviors of the pristine and vacancy-induced Ti2C MXene: Effect of temperature, strain rate, and chirality, Heliyon 10(4) (2024).
[19] S.A. Kazemi, Y. Wang, Super strong 2D titanium carbide MXene-based materials: a theoretical prediction, Journal of Physics: Condensed Matter 32(11) (2019) 11LT01.
[20] S. Wang, J.-X. Li, Y.-L. Du, C. Cui, First-principles study on structural, electronic and elastic properties of graphene-like hexagonal Ti2C monolayer, Computational Materials Science 83 (2014) 290-293.
[21] T. Hu, J. Yang, W. Li, X. Wang, C.M. Li, Quantifying the rigidity of 2D carbides (MXenes), Physical Chemistry Chemical Physics 22(4) (2020) 2115-2121.
[22] Q. Wan, S. Li, J.-B. Liu, First-principle study of Li-ion storage of functionalized Ti2C monolayer with vacancies, ACS applied materials & interfaces 10(7) (2018) 6369-6377.
[23] Y. Wang, J. Xue, G. Nie, X. Guo, Uranium adsorption on two-dimensional irradiation resistant MXenes from first-principles calculations, Chemical Physics Letters 750 (2020) 137444.
[24] J.D. Gouveia, J.R. Gomes, Structural and energetic properties of vacancy defects in MXene

surfaces, Physical Review Materials 6(2) (2022) 024004.
[25] H. Yin, H.J. Qi, F. Fan, T. Zhu, B. Wang, Y. Wei, Griffith criterion for brittle fracture in graphene, Nano Lett. 15(3) (2015) 1918-1924.
[26] L. Yang, I. Greenfeld, H.D. Wagner, Toughness of carbon nanotubes conforms to classic fracture mechanics, Science advances 2(2) (2016) e1500969.
[27] T.L. Anderson, T.L. Anderson, Fracture mechanics: fundamentals and applications, CRC press2005.
[28] T. Shimada, K. Ouchi, Y. Chihara, T. Kitamura, Breakdown of continuum fracture mechanics at the nanoscale, Sci. Rep. 5(1) (2015) 8596.
[29] T. Shimada, K. Huang, N. Ozaki, B. Jang, T. Kitamura, Beyond conventional nonlinear fracture mechanics in graphene nanoribbons, Nanoscale 12(35) (2020) 18363-18370.
[30] P. Jia, K. Huang, T. Sumigawa, T. Shimada, L. Guo, T. Kitamura, A unified atomic energy release rate criterion for nonlinear brittle fracture in graphene nanoribbons, IJSS 234 (2022) 111260.
[31] J. Wang, X. Ye, X. Yang, M. Liu, X. Li, The applicability and the low limit of the classical fracture theory at nanoscale: The fracture of graphene, Engineering Fracture Mechanics 284 (2023) 109282.
[32] M.S. Elapolu, A. Tabarraei, X. Wang, D.E. Spearot, Fracture mechanics of multi-layer molybdenum disulfide, Engineering Fracture Mechanics 212 (2019) 1-12.
[33] T.L. Anderson, Fracture Mechanics Fundamentals and Applications, 4 ed., CRC Press2017.
[34] N.M. Pugno, R.S. Ruoff, Quantized fracture mechanics, Philos Mag 84(27) (2004) 2829-2845.
[35] N. Pugno, A. Carpinteri, M. Ippolito, A. Mattoni, L. Colombo, Atomistic fracture: QFM vs. MD, Eng Fract Mech 75(7) (2008) 1794-1803.
[36] W. Ramberg, s. William R, Description of stress-strain curves by three parameters, National Advisory Committee for Aeronatics, Washington, 1943, pp. 1-32.
[37] D.P. Rooke, D.J. Cartwright, Compendium of stress intensity factors, HMSO Ministry of Defence, Procurement Executive1976.
[38] M.J. Gillan, Calculation of the vacancy formation energy in aluminium, J. Phys.: Condens. Matter 1 (1989) 689-711.
[39] S.M. Hatam-Lee, A. Esfandiar, A. Rajabpour, Mechanical behaviors of titanium nitride and carbide MXenes: A molecular dynamics study, Appl Surf Sci 566 (2021).
[40] J.D. Gouveia, J.R.B. Gomes, Structural and energetic properties of vacancy defects in MXene surfaces, Physical Review Materials 6(2) (2022).